*promoting access to White Rose research papers*

White Rose
Research Online

**Universities of Leeds, Sheffield and York**
**http://eprints.whiterose.ac.uk/**

---

This is the published version of an article in **Journal of the Atmospheric Sciences, 70 (8)**

White Rose Research Online URL for this paper:

http://eprints.whiterose.ac.uk/id/eprint/76580

---

**Published article:**

Schuster, R, Fink, AH and Knippertz, P (2013) *Formation and Maintenance of Nocturnal Low-Level Stratus over the Southern West African Monsoon Region during AMMA 2006.* Journal of the Atmospheric Sciences, 70 (8). 2337 - 2355. ISSN 0022-4928

http://dx.doi.org/10.1175/JAS-D-12-0241.1

---

*White Rose Research Online*
*eprints@whiterose.ac.uk*

# Formation and Maintenance of Nocturnal Low-Level Stratus over the Southern West African Monsoon Region during AMMA 2006

ROBERT SCHUSTER AND ANDREAS H. FINK

*Institute for Geophysics and Meteorology, University of Cologne, Cologne, Germany*

PETER KNIPPERTZ

*School of Earth and Environment, University of Leeds, Leeds, United Kingdom*

(Manuscript received 30 August 2012, in final form 5 April 2013)

ABSTRACT

The southern parts of West Africa are frequently covered by an extensive deck of shallow, low (200–400 m AGL) stratus or stratocumulus clouds during the summer monsoon. These clouds usually form at night in association with a nocturnal low-level jet (NLLJ) and can persist into the early afternoon hours. Recent work suggests that the stratus deck is unsatisfactorily represented in standard satellite retrievals and state-of-the-art climate models. Here the authors use high-resolution regional simulations with the Weather Research and Forecasting Model (WRF) and observations from the African Monsoon Multidisciplinary Analysis (AMMA) 2006 campaign to investigate (i) the spatiotemporal distribution, (ii) the influence on the shortwave radiation balance, and (iii) the detailed formation and maintenance mechanisms of the stratiform clouds. At least some configurations of WRF satisfactorily reproduce the diurnal cycle of the low-cloud evolution, yielding the following main conclusions: (i) The simulated stratus deck forms after sunset along the coast, spreads inland during the course of the night, and dissipates in the early afternoon. (ii) The average surface net shortwave radiation balance in stratus-dominated regions is about 35 W m$^{-2}$ lower than in those with fewer clouds. (iii) The cloud formation is related to a subtle balance between ''stratogenic'' upward (downward) fluxes of latent (sensible) heat caused by shear-driven turbulence below the NLLJ, cold advection, orographic lifting, and radiative cooling on one hand, and ''stratolytic'' dry advection and latent heating on the other hand.

## 1. Introduction

The prediction of the West African monsoon (WAM) is known to have large uncertainties, particularly on climate time scales (Christensen et al. 2007). Climate models show a large spread in rainfall projections and do not even agree on the sign of precipitation changes in the future (Druyan 2011; Paeth et al. 2011), which hinders the development of adaptation strategies (Boko et al. 2007; Roudier et al. 2011). Recently, considerable progress in the understanding (Lafore et al. 2011) and modeling (Xue et al. 2010; Ruti et al. 2011) of the WAM has been achieved through the African Monsoon Multidisciplinary Analyses (AMMA) project (Redelsperger et al. 2006), which in 2006 carried out the most comprehensive field campaign in West Africa to date (Lebel et al. 2010). Such in situ observations remain a key factor for understanding the WAM and improving its operational forecasting (Fink et al. 2011). Despite advances during the first phase of AMMA (2002–10), some well-known model uncertainties remain: errors in the radiative forcing in the heat-low region over the Sahara (Haywood 2005; Milton et al. 2008), errors in the representation of deep convection in the Sahel (Lafore et al. 2011; Fink et al. 2011), and errors in the seasonal development of, and in the air–sea interaction over, the equatorial cold tongue in the Gulf of Guinea (Brandt et al. 2011).

Recent work (Schrage et al. 2007; Knippertz et al. 2011; Schrage and Fink 2012) involving authors from the present paper has drawn attention to a previously understudied source of uncertainty: the formation of low-level continental stratus and stratocumulus cloud decks over moist southern West Africa between the Sahel and

---

*Corresponding author address:* Robert Schuster, Institute for Geophysics and Meteorology, University of Cologne, Kerpener Str. 13, 50937 Cologne, Germany.
E-mail: schuster@meteo.uni-koeln.de

DOI: 10.1175/JAS-D-12-0241.1

© 2013 American Meteorological Society

Guinea Coast, and the associated error in cloud radiative forcing. Knippertz et al. (2011) documented errors of up to 90 W m$^{-2}$ in the mean daily surface solar irradiance in this region in global climate models used for phase 3 of the Coupled Model Intercomparison Project (CMIP3) with individual models' errors closely related to their low-level stratus cover. The stratus decks frequently cover an extensive region stretching from the Guinea Coast (~5°–6°N) to about 9°–10°N during the night and morning hours (Schrage and Fink 2012). Low-level liquid water clouds are well known to have a large impact on radiative transfer (Turner et al. 2007) and consequently also on the diurnal cycle of convection (Grabowski et al. 2006). Kothe and Ahrens (2010) note a larger sensitivity of the surface radiation balance to the cloud fraction than to surface albedo and temperature over the West African intertropical convergence zone (ITCZ) and maritime stratocumulus region off the Angolan coast, but did not explicitly mention the coastal stratus region of West Africa.

One possible reason for the little attention paid to the low continental stratus over West Africa is the difficulty to effectively monitor these clouds at night. The widely used International Satellite Cloud Climatology Project (ISCCP) dataset dramatically underestimates the extensive coverage of very low clouds owing to the small contrast in infrared radiation with the underlying surface (Knippertz et al. 2011). To circumvent this problem, Knippertz et al. (2011) and Schrage and Fink (2012) used a slightly modified version of the ''night microphysical'' scheme from Lensky and Rosenfeld (2008) to visualize the stratus deck at night, based on three infrared channels of Meteosat Spinning Enhanced Visible and Infrared Imager (SEVIRI). However, Knippertz et al. (2011) also documented problems in low-cloud detection due to mid- or high-level clouds in SEVIRI and *Cloud–Aerosol Lidar and Infrared Pathfinder Satellite Observations* (*CALIPSO*) data and due to ground clutter in *CloudSat* data. Stein et al. (2011) used a combined *CloudSat–CALIPSO* product to create a vertical cloud climatology and found nocturnal low-level clouds to occur during 50% of the nights between June and September, which appears to be biased low compared to synoptic reports analyzed by Schrage and Fink (2012). Consequently, eye observations from the comparably sparse synoptic station network in West Africa remain a very important source of low-level cloud information at night, especially in terms of long-term climatologies (Schrage et al. 2007; Schrage and Fink 2012).

Schrage and Fink (2012) present a first analysis of the dynamical processes involved in the formation of the low-level clouds using radiosonde, ceilometer, and wind-profiler measurements performed during AMMA 2006. They suggest that shear-driven turbulence underneath the nighttime low-level jet (NLLJ) causes upward mixing of moisture and therefore favors cloud formation. Bonner and Winninghoff (1969) and Zhu et al. (2001) document a similar effect for the southern U.S. Great Plains. The NLLJ is a typical feature of the stable nocturnal boundary layer, which was first theoretically explained by Blackadar (1957) using ideas of inertial oscillations [see also recent refinement by van de Wiel et al. (2010)]. NLLJs in the WAM region have been documented and discussed by Parker et al. (2005), Lothon et al. (2008), Abdou et al. (2010), Bain et al. (2010), Schrage and Fink (2012), and others.

The main aim of this paper is to complement and expand previous, predominantly observational studies on the West African low-level stratus using high-resolution regional simulations with the Weather Research and Forecasting Model (WRF), which allows a quantification of the relative importance of the different physical processes involved in the cloud formation and maintenance. The main focus will be on the spatiotemporal characteristics of the stratus deck and the role of the NLLJ during the boreal summer months of July–September (JAS) 2006, for which AMMA observations and reanalysis are available as drivers and for validation. An additional aim is to investigate the impact of the stratus deck on the surface net shortwave (SW) radiation balance and temperatures.

Section 2 of this paper describes WRF and the datasets used to initiate and evaluate it. A best-performing model configuration is determined in section 3 together with a model evaluation. The main results are discussed in section 4, which covers the spatiotemporal distribution of the stratus deck, its impact on the surface SW radiation balance, and the relationship to the NLLJ. Main findings are discussed in section 5.

## 2. Model configuration and data

### a. WRF

The nonhydrostatic regional WRF, version 3.3.1, with the Advanced Research WRF (ARW-WRF) dynamical core (Skamarock et al. 2008) was used to analyze the contributions of different processes to the formation of low-level stratus clouds over southern West Africa. The large variety of parameterization schemes available allows identifying a best-performing configuration for the simulation of low-level clouds, which are expected to critically depend on subgrid-scale physics, through a series of sensitivity experiments (see section 3). Parameters common to all experiments are as follows:

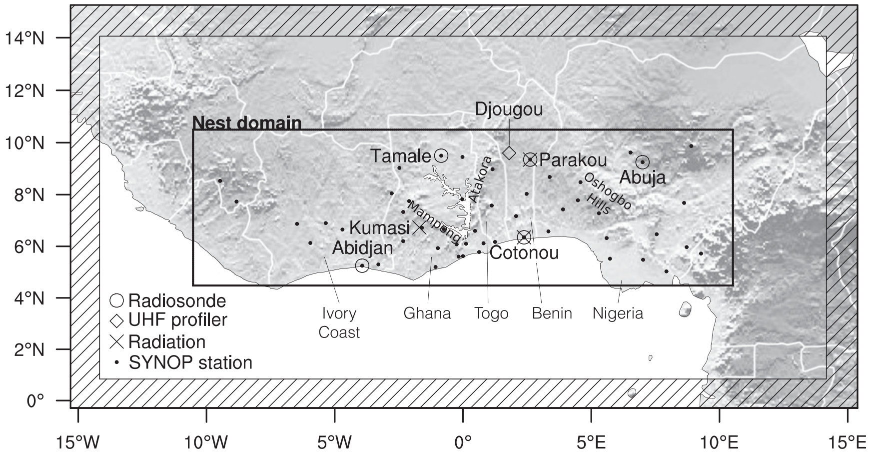

FIG. 1. Study area with the outer and inner model domains; the surrounding hatched area was used for boundary-condition nudging. Locations of in situ measurements are indicated by symbols (circle = radiosonde station, diamond = UHF profiler, cross = radiation measurement, dot = synoptic station) and the orography is shaded.

The model domain comprises an area from 0° to 15°N and from 15°W to 15°E with a two-way nested inner domain covering the main area of interest from 5° to 10°N and from 10°W to 10°E (Fig. 1). The parent (nested) domain has 380 × 195 (781 × 226) grid points and a horizontal grid spacing of 9 (3) km. The top pressure of the domain is 30 hPa with vertical velocity damping in the uppermost 5000 m enabled. The time step is 30 s in the parent and 10 s in the nested domain. The Grell–3D parameterization for convection, which is an improved version of the Grell–Dévényi scheme (Grell and Dévényi 2002), is only used for the coarser domain.

The initial and boundary conditions for each model run in the study period JAS 2006 were taken from the European Centre for Medium-Range Weather Forecasts (ECMWF) AMMA reanalysis, which was created assimilating additional measurements from the AMMA special observation period from May to September 2006 such as 6063 radiosonde profiles, 211 dropsonde profiles, and 7317 pilot measurements (Agustí-Panareda et al. 2010). WRF was initiated at 1200 UTC on each day of the study period and integrated over 54 h. This way the diurnal cycle of stratus formation and dissipation is covered twice in each model run. Boundary conditions were updated every 3 h. The first 6 h of each model run were nudged to the reanalysis in the entire domain with a nudging coefficient of 0.0003 $\mathrm{s}^{-1}$ and ramping within the sixth hour. To specifically investigate subgrid-scale processes involved in the formation of the low-level clouds, additional variables such as accumulated temperature and moisture tendencies from the boundary layer, the radiation, and the microphysics schemes, as well as from grid-scale advection were output for the lowest 20 model layers corresponding to the layer between the surface and roughly 1800 m AGL.

### b. *Data for validation*

Extensive in situ measurements performed during the AMMA special observing period (SOP) 2006 were used to assess the quality of the simulations. This dataset contains reports from synoptic stations and data from radiosondes, pyranometers, a ceilometer, and an ultrahigh-frequency (UHF) wind profiler (see Fig. 1 for locations). Standard surface synoptic observations (SYNOPs; WMO 2010) are the most valuable data sources with regard to fraction of low clouds. Most weather stations across the region are manned with trained observers 24 h $\mathrm{day}^{-1}$. For the JAS 2006 period 8445 reports from 51 stations were available. For Benin and Ghana, the gaps in the Global Telecommunications System (GTS) SYNOP data were filled from archives of the national weather services (for Ghana 0600 UTC only). The variables used for validation are low-level cloud fraction (from part III of the FM12 SYNOP code), temperature and dewpoint at 2 m, mean sea level pressure (MSLP), and wind at 10 m. During the AMMA 2006 field campaign, the radiosonde network was enhanced substantially (Parker et al. 2008). High-resolution wind profiles were taken from radiosonde stations in Abidjan, Abuja, Cotonou, Parakou, and Tamale (see Fig. 1). For the JAS 2006 period 1427 radiosonde profiles were available as raw data with a temporal resolution of 2 s. Measurements of SW and longwave (LW) up- and downwelling radiation were performed in Cotonou and in Parakou (both in Benin) by the Global Change and Hydrological Cycle (GLOWA) project "An Integrated Approach to the Efficient Management of

Scarce Water Resources in West Africa'' (IMPETUS) (Pohle et al. 2010). The instruments used are net radiometers of the type CNR1 from Kipp and Zonen with an International Organization for Standardization (ISO) Second Class pyranometer. These data are available with a temporal resolution of 10 min.

In addition, ground-based remote sensing was used for the validation. The UHF profiler in Nangatchori (close to Djougou, Benin) provides wind profiles with a vertical resolution of 75 m, but because of ground clutter (Jacoby-Koaly et al. 2002) the lowermost level used is at 224 m AGL. A ceilometer was deployed at the same location (Pospichal and Crewell 2007). The bases of up to three cloud layers detected from the backscatter coefficient were used from the ceilometer in the present study. They were averaged over 30 min to get values that we consider to be comparable to eye observations at synoptic stations. A highly inhomogeneous cloud distribution or calm conditions may lead to errors with this method. Satellite-based estimations of surface irradiation or low-level cloud cover are not used for model evaluation owing to systematic errors in this region as documented in Knippertz et al. (2011).

## 3. Identification of a best-performing model configuration

A number of sensitivity tests were conducted with WRF to identify a best-performing model configuration. Because of the large computational cost, the tests were only performed for the 10-day period 18–27 July 2006, which was characterized by frequent nocturnal low clouds. Differences between the experiments were assessed with widely used (skill) scores calculated with respect to in situ observations and evaluated in relation to the ECMWF AMMA reanalysis after regridding the model output (see the appendix for details). Evaluated variables are the fraction of low clouds (CL), MSLP, 2-m temperature ($T_{2\mathrm{m}}$) and humidity ($Q_{2\mathrm{m}}$), 10-m wind speed, the NLLJ {maximum wind speed below a $\sigma$ level [$\sigma$ = pressure/(surface pressure)] of 0.9; $\mathrm{FF}_{\mathrm{max}}$}, and the surface downwelling LW and SW irradiation. WRF calculates cloud fraction based on relative humidity, liquid, and ice water content (Hong et al. 1998). The random-overlap method (Morcrette and Fouquart 1986) was applied to model layers below $\sigma = 0.8$ to calculate CL. Because of the tendency of CL to cluster near 0% and 100% and the different treatment in model and observations, the contingency table–based measures frequency bias (FBIAS) and Peirce skill score (PSS) were calculated using a binary event with a threshold of 50%. The evaluation results for CL during night hours are largely independent of the chosen threshold of 50%; differences only become visible during the afternoon hours, which are not in the focus of the current study. All (skill) scores were finally combined to a single score giving the largest weight to the reproduction of the observed climatology of low-level clouds.

The following parameters/schemes were tested in six experiments in WRF (see overview and explanation of abbreviations in Table 1):

- Experiment 1: Six planetary boundary layer (PBL) schemes with different local and nonlocal closure assumptions in combination with different land surface models (LSMs). All schemes underestimate CL and tend to deteriorate on the second day, but Yonsei University (YSU), Mellor–Yamada–Janjic (MYJ), quasi-normal scale elimination (QNSE), and Mellor–Yamada–Nakanishi–Niino level 2.5 (MYNN2) produce a satisfactory diurnal cycle (Fig. 2a) and a realistic NLLJ (not shown). Following experiments were performed with the MYNN2 scheme (lowest biases in CL and $\mathrm{FF}_{\mathrm{max}}$).
- Experiment 2: Total number of layers of 60, 70, and 80 with 11, 20, and 30 layers below $\eta = 0.8$ (about 1.8 km above ground; $\eta$ is the terrain-following vertical coordinate of WRF). Higher vertical resolution reduces the underestimation of CL (Fig. 2b) but has only a small influence on surface pressure, temperature, humidity, and wind speed, as well as the NLLJ. As the improvement with 80 layers is small, 70 layers are used in following simulations.
- Experiment 3: Three different LSMs using different physical assumptions as well as number and thickness of soil layers. While the performance of Noah and Rapid Update Cycle (RUC) with respect to CL is comparably good (Fig. 2c), the former shows a better diurnal cycle in specific humidity (not shown) and was therefore chosen for further tests. Pleim–Xiu (PX) has lower skill for CL but outperforms the others with respect to surface pressure, temperature, and humidity. The poor performance of the Asymmetric Convective Model, version 2 (ACM2), PBL scheme (Fig. 2a) might be due to the usage of PX.
- Experiment 4: Five microphysics schemes of different complexity. Four of the five schemes show similar performance (Fig. 2d) in good agreement with Otkin and Greenwald (2008) for cloud properties within the PBL. The Morrison and Lin schemes were selected for the final set of experiments. The reason for the bad performance of WRF double-moment 6-class microphysics scheme (WDM6) (FBIAS of 0.52 for CL) appears to be the default initial cloud condensation nuclei (CCN) number concentration of 100 $\mathrm{cm}^{-3}$. An additional run with a more typical value of 1000 $\mathrm{cm}^{-3}$ (Yum and Hudson 2002) improved the performance, but as WDM6 has no sources of CCNs (Lim and Hong

TABLE 1. Overview of the model configurations discussed in sections 3b and 3c. The parameterizations used are as follows: 1) PBL: YSU, MYJ, QNSE, MYNN2, ACM2, and the Bretherton–Park/UW TKE scheme of the University of Washington (UW). UW was used with the Eta similarity surface layer and all others with their corresponding surface layer schemes. ACM2 was used with the Pleim–Xiu LSM and all others with the Noah LSM. 2) LSMs: Noah, RUC, and PX. The Noah LSM employs the Moderate Resolution Imaging Spectroradiometer (MODIS)-based land-use classification; the other two use the United States Geological Survey (USGS) dataset. 3) Microphysics: Lin–Purdue (Lin), Eta–Ferrier (Eta), Stony Brook University (SBU–YLin), Morrison double moment (MOR2), and WDM6. 4) Radiation: GFDL (SW+LW), Dudhia (SW) + RRTM (LW), and RRTMG (SW+LW). References to the parameterization schemes can be found in Skamarock et al. (2008) and in the WRF user guide (Wang et al. 2011).

| Configuration | Expt 1: Planetary boundary layer | Expt 2: Vertical resolution | Expt 3: Land surface model | Expt 4: Microphysics | Expt 5: Radiation transfer | Expt 6: Further test runs | Expt JAS: Best-performing configuration |
|---|---|---|---|---|---|---|---|
| Horizontal resolution (parent, nested) (km) | 9, 3 | 9, 3 | 9, 3 | 9, 3 | 9, 3 | 9, 3 | 9, 3 |
| Vertical resolution | 60 layers, 11 below $\eta = 0.8$ | 60, 70, 80 layers; 11, 20, 30 below $\eta = 0.8$ | 70 layers, 20 below $\eta = 0.8$ | 70 layers, 20 below $\eta = 0.8$ | 70 layers, 20 below $\eta = 0.8$ | 70 layers, 20 below $\eta = 0.8$ | 70 layers, 20 below $\eta = 0.8$ |
| Boundary layer | YSU, MYJ, QNSE, MYNN2, ACM2, UW | MYNN2 | MYNN2 | MYNN2 | MYNN2 | MYNN2 | MYNN2 |
| Land surface model | Noah, PX | Noah | Noah, RUC, PX | Noah | Noah | Noah, PX | Noah |
| Microphysics | WDM6 | WDM6 | WDM6 | Lin, Eta, SBU–YLin, MOR2, WDM6 | MOR2 | Lin, MOR2 | MOR2 |
| Radiation transfer | RRTMG | RRTMG | RRTMG | RRTMG | GFDL, Dudhia–RRTM, RRTMG | RRTMG | RRTMG |
| Convection (only parent domain) | Grell 3D | Grell 3D | Grell 3D | Grell 3D | Grell 3D | Grell 3D | Grell 3D |

2010), the concentration was much reduced on the second simulation day, which is also seen in Figs. 2a–c, as WDM6 was used for all previous tests.

- Experiment 5: Three sets of LW and SW radiation schemes with different numbers of spectral bands, treatment of $CO_2$ and $O_3$, and assumptions on overlapping clouds. The radiation scheme of the Geophysical Fluid Dynamics Laboratory (GFDL) leads to an overestimation of CL (Fig. 2e) and surprisingly to a positive bias in downwelling SW radiation, possibly owing to biases in clear-sky radiation. The Dudhia–Rapid Radiative Transfer Model (RRTM) performs well for CL, but has a bias of $-21.9\,\mathrm{W\,m^{-2}}$ in the downwelling SW radiation. The overall best performance was obtained with the Rapid Radiative Transfer Model for GCMs (RRTMG).
- Experiment 6: The LSM runs were repeated with the two best microphysics schemes, Lin and Morrison, all using MYNN2 PBL, 70 vertical levels, and RRTMG radiation. Again, the influence of varying the microphysics scheme is small (Fig. 2f) and the PX LSM produces too little CL, but the underestimation is smaller compared to the run using PX with WDM6 (Fig. 2c). CL is overestimated with RUC, likely because of unrealistically large specific humidity changes. Therefore it was decided to use the Noah and Morrison schemes (Table 1). It is worthwhile to note that because of the large weight of CL in the evaluation, this configuration might not be optimal for the investigation of other aspects.

Using the identified best-performing model configuration, 90 model runs were conducted for the period JAS 2006—one for each day starting on 1200 UTC and integrated for 54 h. The resulting mean diurnal evolution of CL is close to observations (Fig. 3a) with an FBIAS value of 1.07. The minimum is reached at 1800 UTC in the model but at 2100 UTC in the observations, for which, however, only a small number of synoptic reports is available. The relatively small PSS for CL suggests that day-to-day variations are not well captured. The bias in the incoming SW radiation of $-16.8\,\mathrm{W\,m^{-2}}$ (Fig. 3f) points to problems with the optical thickness of the clouds. The 2-m temperature and specific humidity have clear negative biases (Figs. 3b and 3c) while the 2-m relative humidity is well represented (Fig. 3d). The temperature bias of $-1.74$°C is consistent with the SW radiation bias. The specific humidity bias increases from around $-0.5$ to about $-2.1\,\mathrm{g\,kg^{-1}}$. Such a dry bias was also found during the creation of the AMMA reanalysis, which was corrected by increasing the soil moisture (Agustí-Panareda et al. 2010). The drift in WRF toward a drier state is likely connected to the chosen LSM despite its overall best performance and may also explain

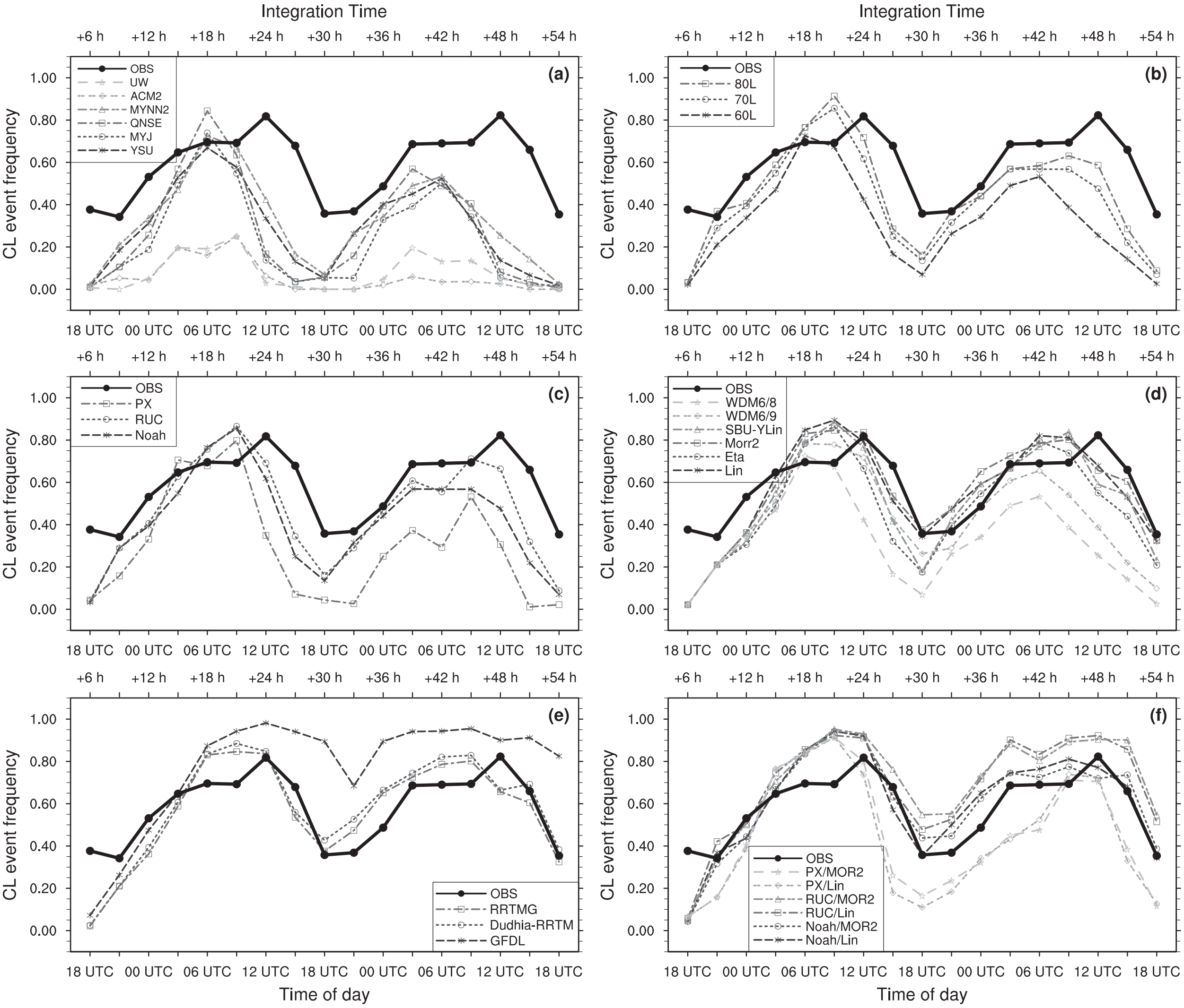

FIG. 2. Frequency of the binary event ''low-level cloud cover larger than 50%'' plotted against (a) the integration time for the boundary layer experiment, (b) the vertical resolution experiment, (c) the land surface model experiment, (d) the microphysics experiment, (e) the radiation experiment, and (f) for the best-performing configuration experiment. OBS is the observed frequency from synoptic stations and a ceilometer in Djougou. WDM6/8 is WDM6 with an initial CCN concentration of 100 $\mathrm{cm}^{-3}$, and WDM6/9 is WDM6 with an initial CCN concentration of 1000 $\mathrm{cm}^{-3}$.

the bias in downwelling LW radiation (Fig. 3e). All further analysis is limited to the first integration day in order to reduce the impact of this drift.

The simulated wind profiles were compared to radiosondes and the UHF at Djougou (see Fig. 1 for locations). Analyzed times are 2300 UTC (+11 h) and 0500 UTC (+17 h), as radiosondes are usually launched up to 1.5 h before the synoptic hours (e.g., U.S. National Weather Service 2010). For the coastal stations Abidjan (2300 UTC only) and Cotonou the model overestimates the maximum wind speed and the stability in the lowest few hundred meters with the core of the simulated NLLJ too low (Figs. 4a and 4c). The inland station Abuja has a relatively low frequency of stratus clouds and both model and observations show a weaker NLLJ with a maximum too close to the ground in the model at 2300 UTC (Fig. 4b). Parakou at a comparable distance to the coast is cloudier and the observed and simulated NLLJs are more pronounced and closer to the ground (Fig. 4d). Tamale has less frequent and less extensive stratus cloud cover. The model overestimates the wind speed of the NLLJ maximum but represents well the wind shear underneath the jet (Fig. 4e). Agreement between the measurements in Djougou and the simulation is reasonable at 2300 UTC but large deviations are visible at 0500 UTC. Possible reasons include the lower altitude in the model by about 70 m and errors in the UHF wind measurements close to the ground.

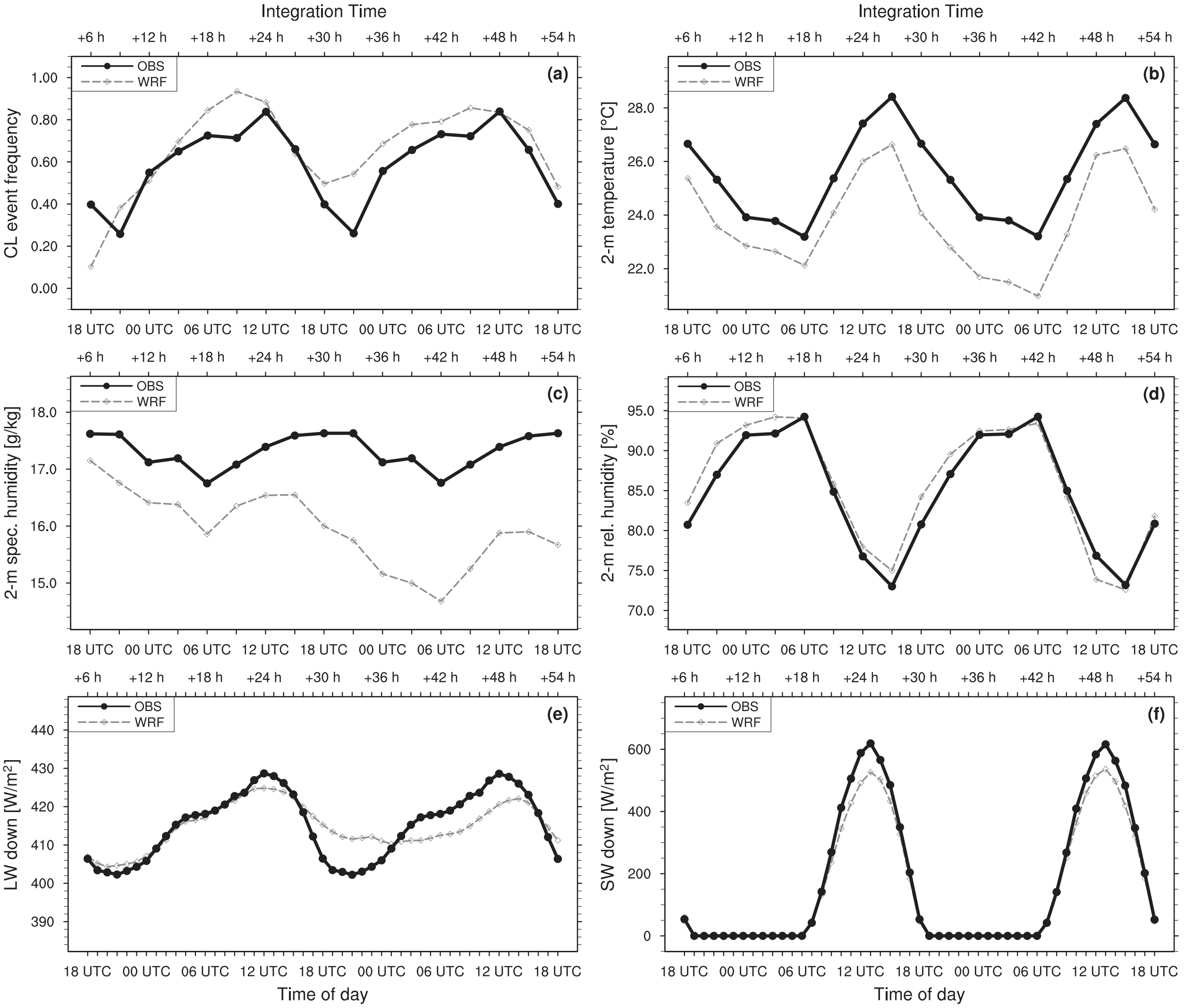

FIG. 3. Evaluation of the 90 daily model runs during the period JAS 2006. Shown is (a) the frequency of the binary event ‘‘low-level cloud cover larger than 50%’’ with the observed frequency from synoptic stations and a ceilometer in Djougou, (b) the 2-m temperature, (c) the 2-m specific humidity, (d) the 2-m relative humidity, (e) the downwelling longwave radiation, and (f) the downwelling shortwave radiation. OBS in (b),(c),(d) is the corresponding mean value from synoptic stations; OBS in (e),(f) is the corresponding mean values from measurements in Cotonou and Parakou.

## 4. Results

### a. *Spatiotemporal distribution of low-level clouds in WRF*

As shown in section 3, the diurnal cycle of low-level cloud cover in the whole domain is well represented by the model with a minimum at 1800 UTC (Fig. 3a). The spatial distribution reveals a first cloud increase along the coastline after sunset and then a spreading inland during the course of the night (Figs. 5a–e). This is consistent with the observed late stratus onset at the inland station Djougou around 0236 UTC (Schrage and Fink 2012). An unexpected result is the large simulated cloud fraction over the Gulf of Guinea during day and night, consisting of maritime stratus, but also of a shallow layer of mist (visibility under 8 km and relative humidity above 80%) or fog (visibility under 1 km). A closer inspection, not illustrated here, revealed that this layer is limited to the lowest model levels and shows liquid water contents of less than 0.1 g m$^{-3}$ (0600 UTC) on average, which corresponds to a visibility of 200 m or more (Gultepe et al. 2006). There are regular reports of mist at 0600 UTC from Lagos (Nigeria) and Accra (Ghana), but not of fog. The average liquid water path is smaller than 20 g m$^{-2}$ at 0900 UTC and smaller than 10 g m$^{-2}$ at 1200 UTC; accordingly, the modeled effect

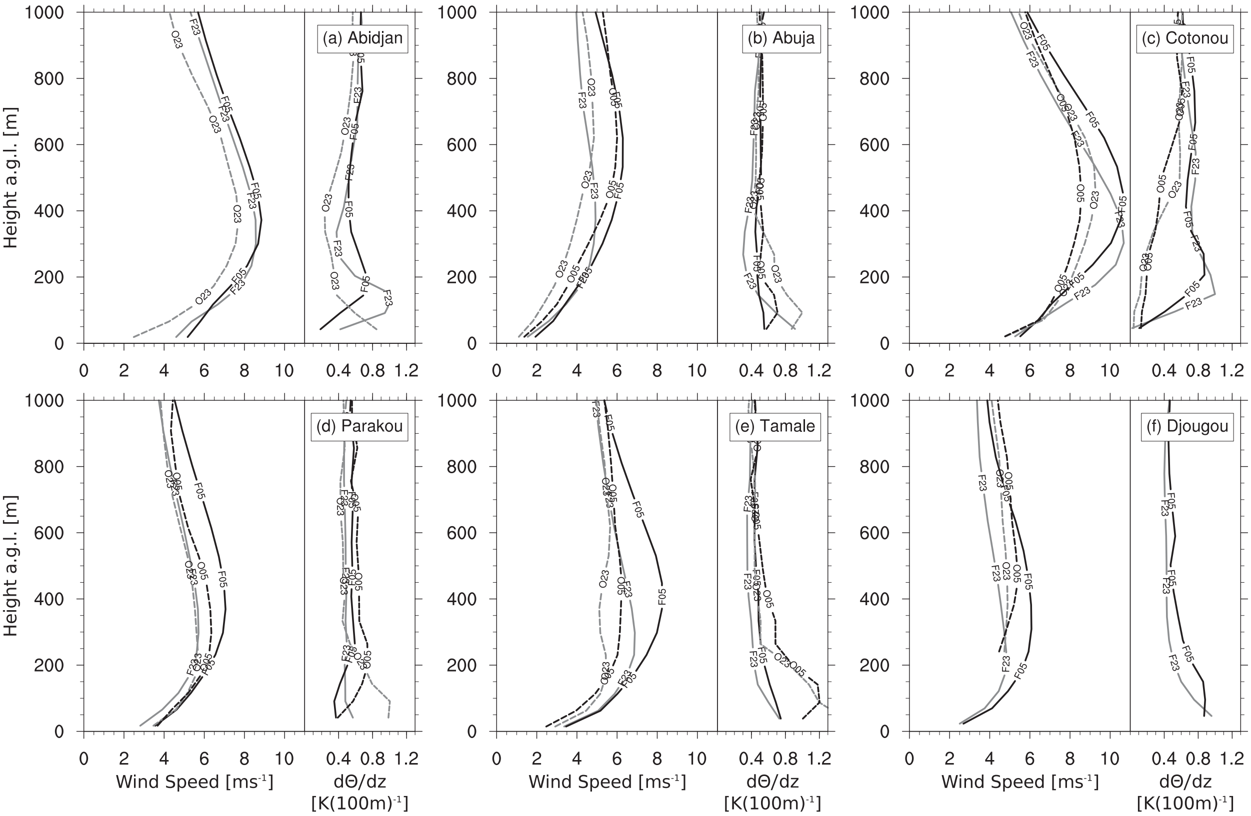

FIG. 4. In each panel, (left) averaged wind and (right) stability profiles for the time period JAS 2006 from the WRF simulations (solid lines), (a)–(e) from radiosondes (dashed lines), and (f) from the UHF profiler in Djougou (dashed lines). Shown are the wind speed and stability in the lowest 1000 m AGL at 2300 UTC (gray lines) and 0500 UTC (black lines). Only dates with observation and simulation available were considered for averaging. The observations are vertically averaged to the model layers. The lowest observations from the UHF profiles were not used because of ground clutter.

on the SW radiation balance is small and this aspect was not further investigated.

A striking effect is the influence of low mountain ranges on the stratus deck, best identified at 0600 UTC (Fig. 5e). The stratus extends up to a few hundred kilometers between the coastline and the windward side of the mountains but quickly dissolves at the lee side. This foehn effect is most pronounced where the mountain ranges are orthogonal to the average direction of the low-level flow like the Mampong Range in Ghana or the Oshogbo Hills in Nigeria southwest of the River Niger (for location, see Fig. 1). Such sharp edges are also often visible in nighttime Meteosat SEVIRI red–green–blue (RGB) images (not shown). The maximum domain-averaged cloud cover is reached shortly after sunrise around 0900 UTC (Fig. 5f; see also Fig. 3a). Afterward, the cloud deck gets increasingly fragmented by enhanced thermal turbulence, which also causes the formation of daytime cumulus or stratocumulus in the previously cloud-free regions farther to the north—for example, in the north of Ghana. The cloud fraction is usually lower in this region and the cloud base above ground is higher.

### b. Impact of low-level clouds on shortwave radiation

The spatial distribution of low-level clouds in the model (Fig. 5) is reflected in the SW radiation balance at the surface (Fig. 6a). On average, cloudier regions (here defined as grid points with a time-averaged cloud fraction of more than 50%) show low downwelling SW radiation of 133 W m$^{-2}$—much lower than the domain average of 159 W m$^{-2}$ and the value for less cloudy regions (here defined as grid points with a time-averaged cloud fraction of less than 50%) of 198 W m$^{-2}$. While the latter is consistent with an observed long-term mean value (2001–07) at the often cloud-free station Cotonou of 198 W m$^{-2}$, the mean value for cloudy regions appears rather low compared to additional observations shown in Knippertz et al. (2011) not available for 2006. Kumasi (Ghana), which is located in one of the most frequently cloud covered regions south of the Mampong Range, reaches a mean observed value of 147 W m$^{-2}$

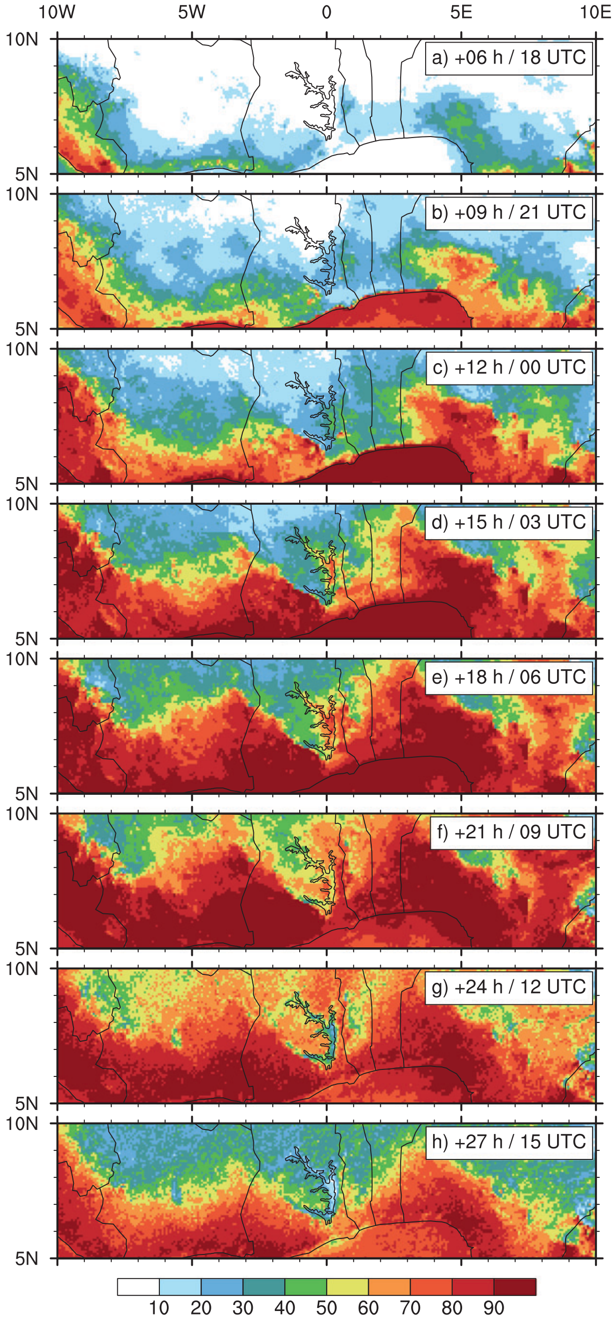

FIG. 5. Spatial distribution of low-level cloud cover (%) averaged over 90 daily model runs during the period JAS 2006.

during JAS 2010, while the few other stations in the region show even higher values. This negative bias is consistent with the findings in section 3 and possibly related to a too optically thick stratus in the model. A detailed analysis of this important aspect, however, is beyond the scope of this paper and left for future study.

The simulated mean value of the net SW radiation balance in cloudier regions is 90 W m$^{-2}$ and in less cloudy regions is 125 W m$^{-2}$. This difference is substantial and leads to a reduction of the daily mean 2-m temperature of 2.2°C and of the daily maximum temperature of 4.1°C. Temperature differences on this order of magnitude are sufficient to set up regional circulations and to make the difference between favorable and nonfavorable conditions for convection. Using large-eddy simulations, Garcia-Carreras et al. (2011) found that temperature differences as small as 1 K caused by heterogeneity in surface fluxes over different land surfaces on scales of tens of kilometers can create enough convergence to trigger convective clouds. In addition, the colder cloudier regions are located south and thus upstream of the warmer regions with respect to the primary southwesterly flow, which leads to advection of colder air over warmer ground—a situation where the warmer air is lifted and the static stability in the upper boundary layer is reduced (Baldi et al. 2008).

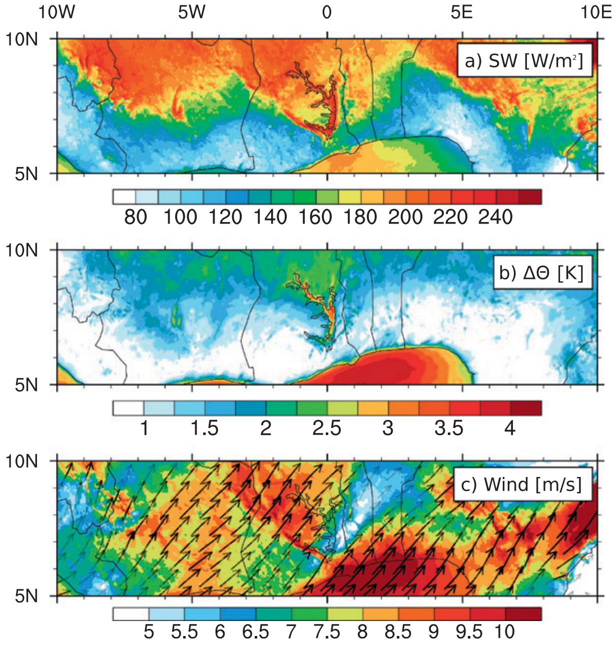

FIG. 6. (a) Simulated downwelling shortwave radiation at the ground (W m$^{-2}$), averaged over the 24-h period from 0000 to 0000 UTC, and 90 daily model runs during JAS 2006. (b) Average difference in potential temperature between the first and the sixth model layer (~300 m AGL) at 0100 UTC; positive values correspond to an increase with height. (c) Average wind speed maximum below $\sigma = 0.9$ at 0600 UTC given as shading and vectors.

### *c. Relationship between NLLJ and low-level cloud formation*

Mechanical turbulence driven by the wind shear underneath the NLLJ has been proposed as an important factor for stratus formation in West Africa (Knippertz et al. 2011; Schrage and Fink 2012). The importance of shear-driven turbulence was also documented for nocturnal boundary layer clouds in the Great Plains (Zhu et al. 2001). Generally, turbulence is increased when the critical Richardson number $Ri_c = 0.25$ is reached, which depends not only on wind shear, but also on stability. In very stable conditions, more turbulent energy is dissipated by the work against negative buoyancy than is produced by wind shear. This situation is most often simulated in the northern parts of the model domain, which are frequently cloud-free and affected by a strong radiative cooling after sunset, leading to differences of 2–2.5 K in the potential temperature between the first and the sixth model layer (Fig. 6b). The latter is located about 300 m above ground, at typical NLLJ heights. Reaching $Ri_c$ under such conditions would require a wind difference of 9–10 m s$^{-1}$ between the lowest and the sixth model layer, which is not found in the model, nor observed (Fig. 4). Schrage and Fink (2012) discuss a case of a cloud-free night at Djougou at the northern edge of the simulated stratus zone, when the low-level static stability after sunset was higher than usual and stratus did not form. In the stably stratified regions, the NLLJ speed can increase during the night and reach its maximum around sunrise at 0600 UTC (Fig. 6c). The maximum stability in the northern part of the domain is reached around 0100 UTC and is afterward reduced by the advection of cooler air and occasional turbulent mixing related to the NLLJ, but the stratification remains stable on average until sunrise, after which enhanced thermal turbulence erodes the jet.

The radiative cooling of the surface after sunset suppresses mixing in the boundary layer as shown by the turbulent kinetic energy (TKE) within the lowest model layers (Fig. 7a). Only a small strip with higher TKE values along the coast remains, which results mainly from the abrupt change in surface roughness. In the course of the night TKE along the coast increases together with the strengthened NLLJ and the turbulent area spreads farther inland (Figs. 7b and 7c). During individual nights this inland movement is of an almost frontal nature with a clear distinction between turbulent and nonturbulent regions (not shown). Occasional gaps within the turbulent areas suggest intermittent turbulence.

The simulated spatiotemporal distributions of TKE and low-level cloud cover are highly correlated, which supports the conclusion of Schrage and Fink (2012) that turbulent vertical transport of moisture contributes to the formation of the clouds. To further investigate the contributions of other processes, two vertical cross sections parallel to the mean NLLJ directions were created based on averages over all model runs that have a domain-mean low-level cloud fraction of 66% or more at 0600 UTC (55 out of 90). Bringing the cross sections into a line with the NLLJ simplifies the interpretation, as no component of horizontal advection perpendicular to the cross sections needs to be considered. Cross-section I cuts through the Mampong Range in Ghana and cross-section II from coastal Benin to the Oshogbo Hills in Nigeria (see Fig. 7a for the locations). Results are displayed in Figs. 8 and 9. Cross-section I shows one cloud maximum at 0600 UTC between the coast and the mountains (Fig. 8a) while cross-section II has two maxima: one from the coast to about 7.5°N and another around 9°N on the windward side of the mountains (Fig. 8f). We also computed 1800–0600 UTC accumulated temperature and humidity tendencies from the parameterization schemes and grid-scale advection as well as nighttime averages of TKE and wind speed. As the accumulated tendencies are strongly influenced by small-scale orographic features, a 33-gridpoint (~99 km) running mean was applied. The two cross sections show rather different conditions. Cross-section I (Figs. 8 and 9, left columns) shows a situation where turbulent effects and orographically forced lifting are collocated, while both effects are spatially more separated in cross-section II (Figs. 8 and 9, right columns). We will therefore concentrate on the latter in the following discussion.

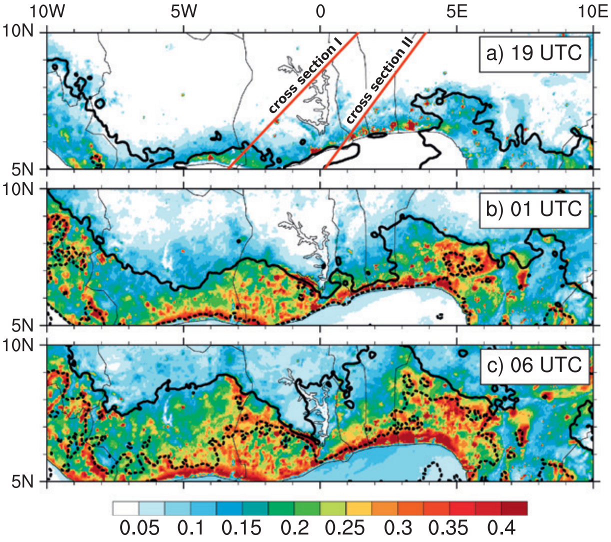

FIG. 7. Mass-weighted average of TKE (m$^2$ s$^{-2}$) over the lowest 10 model layers, temporally averaged over 90 daily model runs during JAS 2006, at (a) 1900, (b) 0100, and (c) 0600 UTC. The cross sections shown in Figs. 8 and 9 are marked in (a). The solid (dashed) black line indicates a low-level cloud cover of 50% (90%).

The strongest wind shear in cross-section II is found within the first 100 km behind the coastline (Fig. 8g), which is also the region where the highest values of TKE are found in a layer of about 300–400-m height (Fig. 8h). The NLLJ speed farther inland is lower and only a very shallow turbulent layer with comparatively low TKE values is simulated. Cross-section I has lower wind speed

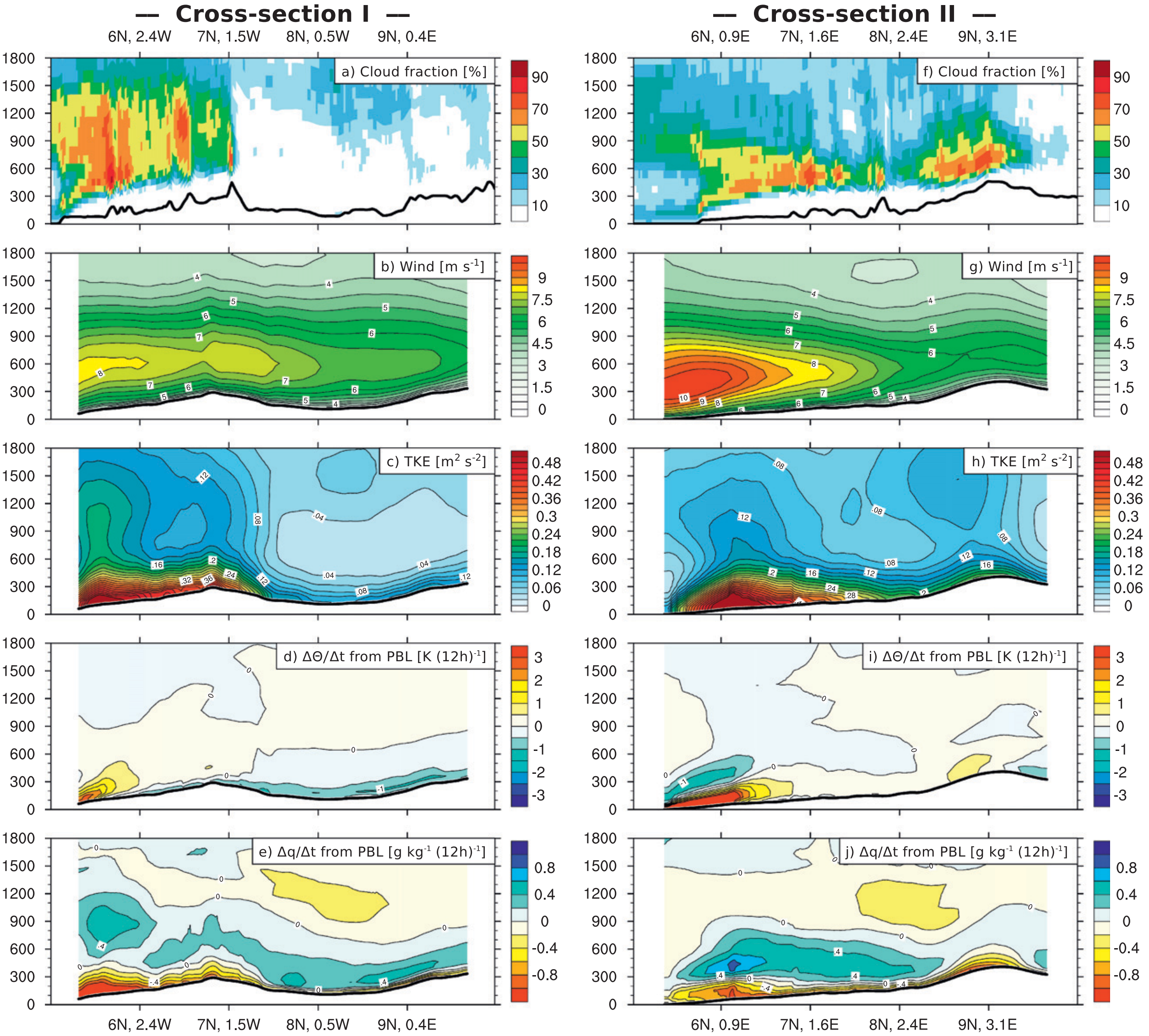

FIG. 8. Vertical cross sections along the red lines shown in Fig. 7a. (a)–(e) Cross-section I and (f)–(j) cross-section II. All values are averages over days when at least 66% of the whole domain is covered by low clouds at 0600 UTC (55 of 90 days). Shown variables are (a),(f) cloud fraction at 0600 UTC; (b),(g) wind speed and (c),(h) TKE, both averaged from 1800 to 0600 UTC; and (d),(i) temperature tendency and (e),(j) and moisture tendency, both from PBL scheme and accumulated from 1800 to 0600 UTC.

values in the south and higher values in the north compared to cross-section II, which is consistent with the higher static stability in the north in this region (Fig. 6b), which suppresses turbulence generation. In both cross sections, the turbulence north of the coast causes a vertical downward directed heat flux, leading to a cooling of about 1 K in 200–300 m above ground and a warming of up to 3 K close to the ground in cross-section II (Figs. 8d and 8i). This effect is connected to the horizontal advection of cold air from the ocean (Figs. 9a and 9e), whose strength and vertical distribution also explains why the heat flux in cross-section II is more pronounced. The vertical gradient in the potential temperature and values of TKE are much smaller in the north, leading to smaller temperature tendencies from vertical mixing. Compared to the heat flux, the upward transport of moisture is visible over a wider area (Figs. 8e and 8j), spanning from the coast to about 8.5°N in cross-section II. The specific humidity close to the ground is reduced by about 0.5 $\mathrm{g\,kg^{-1}}$ and increased by the same amount below the NLLJ. Not surprisingly, the location of the maximum latent heat flux indicated by the largest tendencies in specific humidity is collocated with the TKE maximum. The grid-scale horizontal advection implies an inhibiting effect on cloud formation, caused by a reduction of the specific humidity at the ground as well

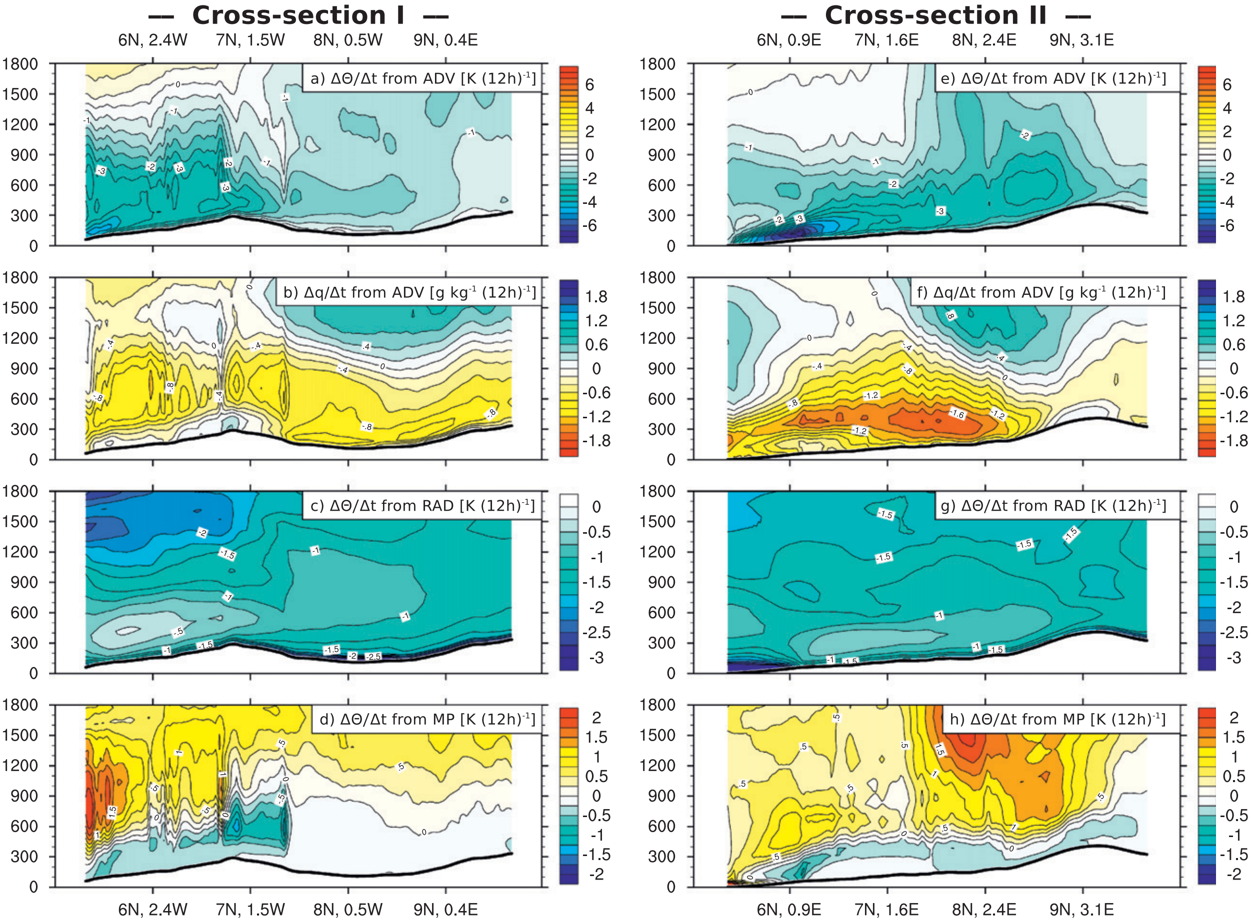

FIG. 9. As in Fig. 8 but for (a),(e) temperature tendency from grid-scale advection, (b),(f) moisture tendency from grid-scale advection, (c),(g) temperature tendency from radiation scheme, and (d),(h) temperature tendency from latent heating, all accumulated from 1800 to 0600 UTC.

as at the jet level. This at a first glance counterintuitive effect, also described by Schrage et al. (2007), is the result of the meridional distribution of specific humidity with a maximum located over the continent between 5° and 15°N, since much of the moisture in the monsoon layer is recycled water from local evaporation (Nicholson 2009). Together with the predominantly southwesterly flow at the Guinea Coast, this distribution leads to an upgradient flow. Other important processes are radiative cooling at the cloud top of about 2 K (Figs. 9c and 9g), which supports cloud formation, and latent heating within the cloud deck of about 1 K (Figs. 9d and 9h), which counteracts this cooling. The net effect of these two processes is a cooling of the stratus cloud layer and thus a contribution to its maintenance once the stratus deck has formed. In addition, entrainment of warmer and drier air, and radiative cooling near the top of the cloud layer have been shown to affect cloud lifetime and properties (Yamaguchi and Randall 2008), but a detailed analysis of these effects is beyond the scope of this paper.

In the following the differences between cloudy and clear nights are further analyzed at 6.2°N on cross-section II. This point is characterized by a maximum in TKE and cloud cover. With the values discussed below, this point is, however, not representative for the whole domain, but well suited to illustrate general differences between clear and cloudy nights. Vertical profiles of tendencies summed up from 1800 to 0600 UTC as shown in Figs. 8 and 9 were calculated for a composite of the 15 clearest (Figs. 10a and 10b) and the 15 cloudiest nights in the model (Figs. 10c and 10d). The main differences between the two cases are related to the PBL scheme. Vertical mixing in cloudy nights is stronger with a larger vertical extent. In clear nights the mean effect of sensible heat flux is a warming of approximately +1.3 K in the lowest 150 m AGL and a cooling of −0.6 K between 150 and 400 m (Fig. 10a). In cloudy nights sensible heat fluxes warm the lowest 300 m by +1.8 K and cool the layer between 300 and 700 m by about −0.8 K (Fig. 10c). The cooling in cloudy nights is supported by stronger

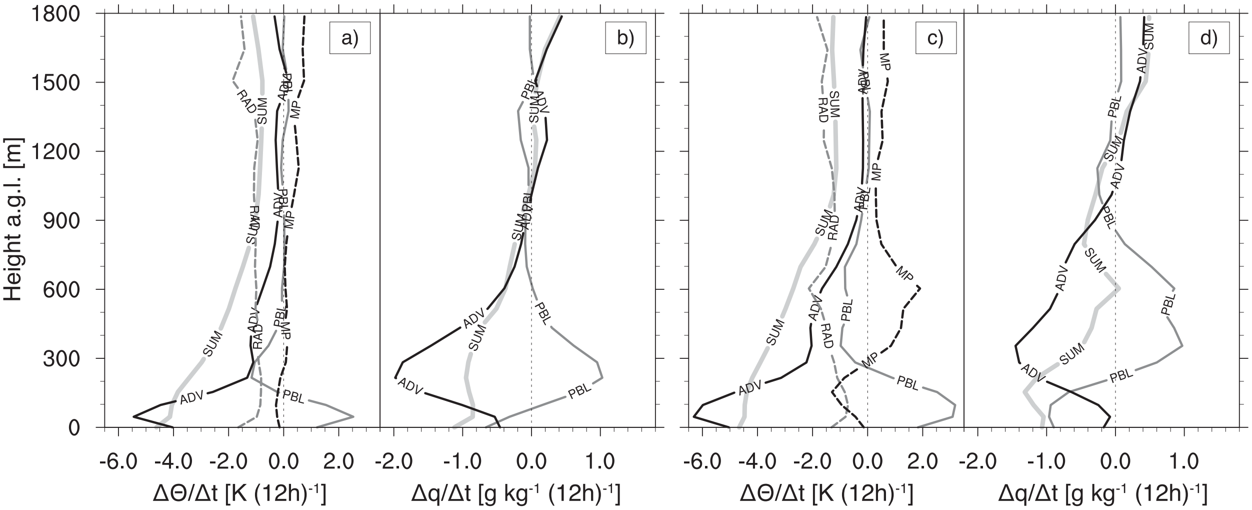

FIG. 10. Vertical profiles of temperature and humidity tendencies summed up from 1800 to 0600 UTC at 6.2°N on cross-section II (see Fig. 7 for location) for (a),(b) the 15 clearest nights and (c),(d) the 15 cloudiest nights. Abbreviations are ADV: advection, PBL: planetary boundary layer scheme, MP: microphysics scheme, RAD: radiation scheme, and SUM: sum of all components.

cold advection up to about 1000 m. Both effects are consistent with a stronger monsoon circulation during cloudy nights. In clear nights, tendencies from the microphysics scheme are expectedly low and radiative cooling cools the lowest 1300 m by an almost constant value of 1 K (Fig. 10a). In cloudy nights, there is significant warming from latent heating in the cloud layer between 300 and 900 m on the order of 1 K, which is more than compensated by enhanced radiative cooling (Fig. 10c). Under the clouds, evaporation of light precipitation leads to a moderate cooling from the microphysics scheme. Tendencies of specific humidity from the PBL scheme are also larger and reach deeper in cloudy nights, which is consistent with the temperature signals. While in clear nights drying due to horizontal advection is much stronger than moistening by vertical mixing (Fig. 10b), the latter is nearly able to compensate the negative effect of advection in cloudy nights (Fig. 10d). The vertically averaged effect of advection is similar in both cases. The main difference is the distribution over a larger column in cloudy nights. Overall, in cloudy nights the layer between 300 and 600 m cools by approximately 1 K more than during clear nights and dries by about 0.3 g kg$^{-1}$ less. These subtle differences are enough to generate saturation during cloudy nights, which further enhances cooling through LW radiative effects.

Figure 11 shows the evolution of cloudiness, NLLJ, wind shear, and stability for the same gridpoint. The 15 clearest nights still reach cloud fractions around 20% in the morning hours with rather little vertical structure (Fig. 11a), while the 15 cloudiest nights show a very sharp increase of cloud fraction in the 300–900-m layer reaching almost 100% around 400 m by 0600 UTC (Fig. 11e). The NLLJ is weaker in clear nights than in cloudy nights, and the height of the maximum is closer to the ground (Figs. 11b and 11f). This is in agreement with an observation-based discussion of a clear night by Schrage and Fink (2012), where also no strong NLLJ was found. As mentioned earlier, the strengths of vertical mixing depends on the static stability and the vertical wind shear. The nighttime evolutions of both quantities differ between clear and cloudy nights. In clear nights, the gradient in potential temperature in the lowest model levels increases until approximately 0000 UTC and is only slightly reduced afterward (Fig. 11d) by mechanical mixing. The vertical wind shear shows a comparable behavior (Fig. 11c). This differs from the conditions farther to the north, where, as mentioned earlier, the wind speed in the NLLJ can increase until sunrise. In cloudy nights, the static stability also increases during the first half of the night, but then the wind shear becomes too strong and turbulence sets in. The vertical gradients in potential temperature and wind speed are reduced and the core of the NLLJ moves upward (Figs. 11f–h) as the mixed layer underneath it thickens. The growing extent of the mixed layer over time is well reflected in the growing thickness of the cloud layer (Fig. 11e).

The discussion above demonstrates the subtle balances between advective, turbulent, radiative, and diabatic processes that ultimately decide between formation and nonformation of the cloud decks.

## 5. Discussion and conclusions

The regional WRF was used to carry out daily 54-h simulations of the West African summer monsoon during

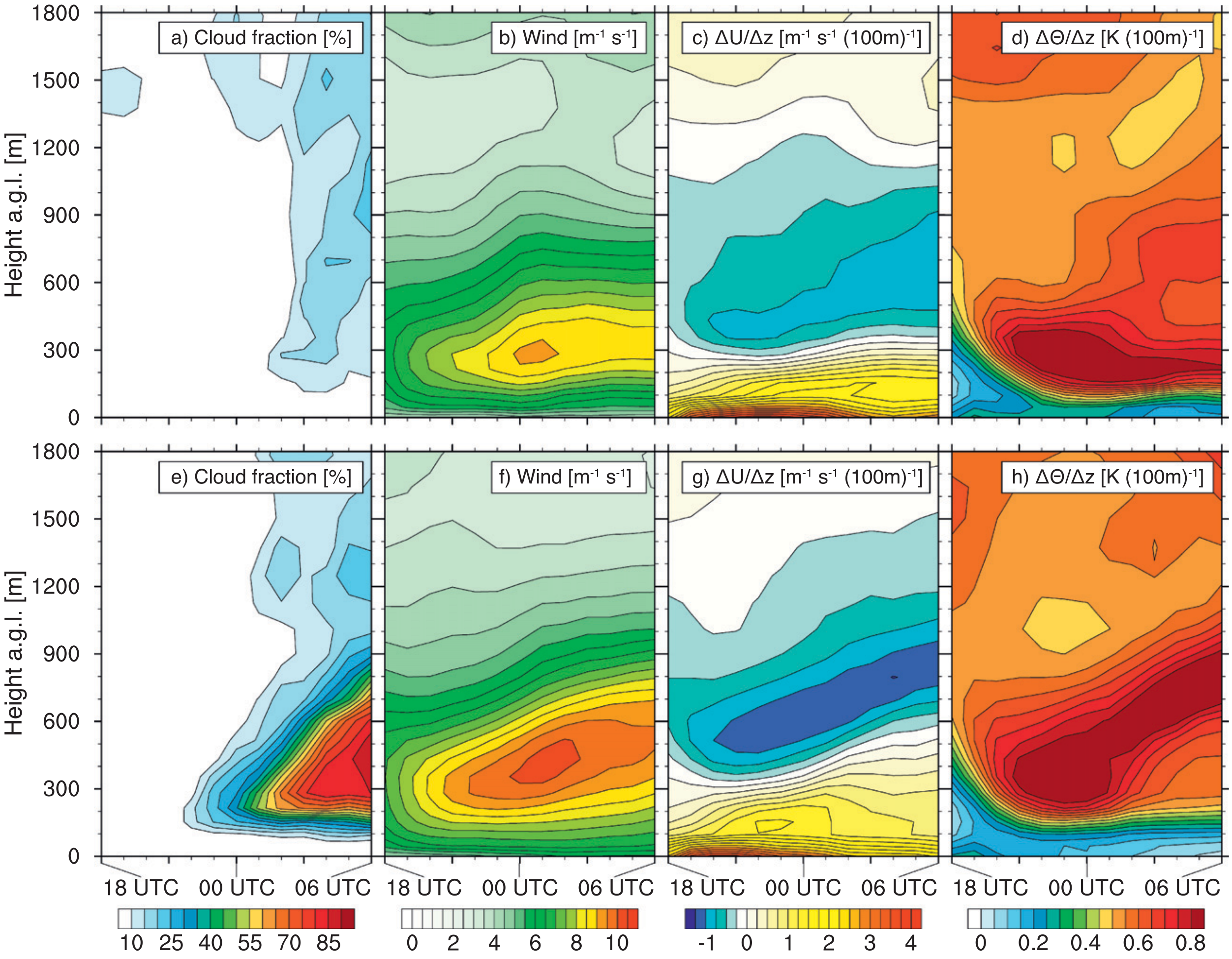

FIG. 11. Temporal evolution from 1800 to 0600 UTC of vertical profiles at 6.2°N on cross-section II (see Fig. 7 for location) for (a)–(d) the 15 clearest nights and (e)–(h) the 15 cloudiest nights. Shown are (a),(e) cloud fraction, (b),(f) the horizontal wind speed, (c),(g) vertical gradient in horizontal wind speed, and (d),(h) vertical gradient in potential temperature.

JAS 2006 in order to verify and refine observation-based ideas of low-level stratus formation proposed by Schrage et al. (2007), Knippertz et al. (2011), and Schrage and Fink (2012). A thorough validation analysis was conducted using a variety of observations, including several thousand eye observations of low-level clouds from synoptic stations and radiosondes from the AMMA 2006 campaign. Low-level cloud formation in WRF was found to be sensitive to the choices of the land surface model, the boundary layer scheme, and the vertical resolution within the boundary layer. With the best-performing configuration given in Table 1, WRF simulates the diurnal evolution of the stratus deck satisfactorily, which lends credence to the interpretation of pertinent stratogenetic processes in the simulations.

The different contributions to the cloud formation process are schematically summarized in Fig. 12, showing both the situation close to the coast and farther inland. The horizontal advection of cooler (but also slightly drier) air is an important factor in both regions. The shear-driven turbulent vertical transport underneath the NLLJ is most pronounced close to the coast where the upward transport of latent heat increases the specific humidity in the cloud level by 0.5 g kg$^{-1}$ while the downward transport of sensible heat decreases the temperature by 1 K. Here, the radiative cooling at the cloud top of about 2 K during the night stabilizes the cloud deck, as it is only partly compensated by latent heating of about 1 K. This process might, however, also mix drier air from above the boundary layer into the cloud deck in some situations, which can create downdrafts through evaporation of cloud droplets. As the stratus usually produces not more than light drizzle, evaporative cooling underneath the cloud deck is only about 0.2 K. There appears to be a competition between the radiative cooling of the surface and the turbulent transport as suggested

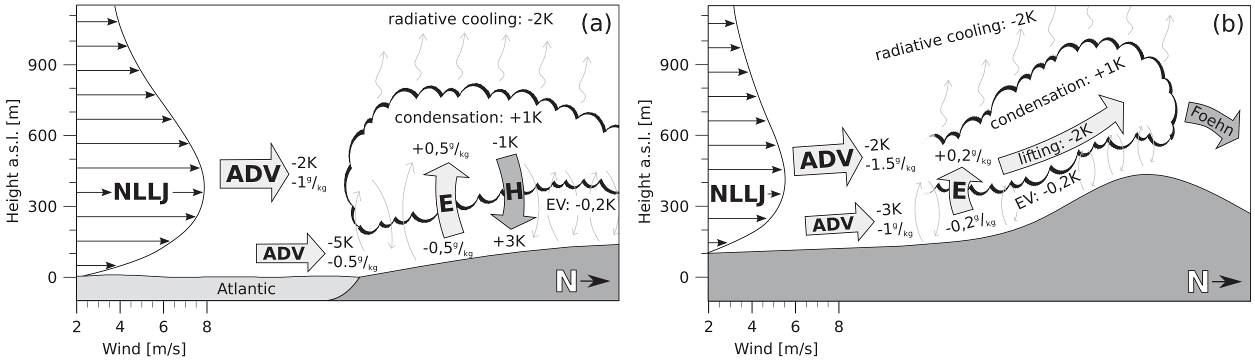

FIG. 12. Schematic illustration of the cloud formation process for (a) conditions close to the coast and (b) farther inland. Abbreviations are ADV: advection, *E*: latent heat flux, *H*: sensible heat flux, EV: evaporation, and NLLJ: nighttime low-level jet. Typical values for the contribution from each process are given. The effect of lifting was estimated by the difference in height and the assumption of a vertical temperature gradient of 0.65 K (100 m)$^{-1}$. Other values are estimated based on cross-section II.

by Schrage and Fink (2012). The cooling of the surface weakens after the cloud deck is formed, which favors further vertical mixing and maintains the cloud deck. In contrast, if the surface cools too fast, the vertical mixing is suppressed and the night remains clear. The latter usually happens northward of low mountain ranges.

Farther away from the coast, even in cloudy conditions, the turbulence is generally not very marked, suggesting that vertical mixing is not the main cause of the cloud cover. Orographically forced lifting at the windward side of mountains creates additional cooling in areas of small vertical mixing and weaker advection of cold air, while the cloud deck immediately dissipates at the leeside, where stable conditions further suppress cloud formation. For this configuration of WRF, it can therefore be concluded that the low-level nocturnal stratus deck over the continent is formed owing to a combination of turbulent vertical mixing driven by the NLLJ, the advection of cool air from the south (which increases with stronger NLLJs), and forced lifting on the windward side of mountains. The contribution of these individual processes varies throughout the model domain, with turbulent processes dominant close to the coast and forced lifting farther inland. Radiative cooling helps to maintain the stratus once it has formed.

This study is the first to quantify the subtle balance between stratogenetic and stratolytic processes in all detail and is therefore an important extension of the work by Schrage et al. (2007), Knippertz et al. (2011), and Schrage and Fink (2012). The results presented here suggest that the problems of many CMIP3 global models in representing the stratus deck are likely not solely related to the coarse vertical resolution in the boundary layer. Instead, small differences in the advected air masses or turbulent fluxes, for example, could be sufficient to lead to a substantial bias in the cloud cover.

The simulated cloud deck is formed after sunset along the entire West African southern coast and spreads farther inland during the course of the night. This is no pure advection by cloud-level winds, but a spreading of turbulent conditions. The dissipation continues into the afternoon hours and the spatiotemporal distribution is clearly reflected in the net SW radiation balance at the surface; its daily average is reduced by about 35 W m$^{-2}$ in the cloudier half of the region relative to the less cloudy half. This effect is also visible in the 2-m temperature with the daily maximum being 4.1°C lower in the former. The altered radiative forcing has some important implications on different scales. Using single-column models, Grabowski et al. (2006) showed that especially in the hours after sunrise the low-level cloud cover is critical for the correct simulation of the diurnal cycle of deep convection, which is triggered too early in the absence of low-level clouds. A similar effect was seen when the best-performing model configuration used in this study was compared to a configuration from the first sensitivity experiment (see section 3) with less stratus cloud cover: the former generated a realistic diurnal cycle, while the latter showed a too-early start of precipitation in the course of the day (not shown). On the larger scale, an adjustment of the meridional overturning is conceivable. Eltahir and Gong (1996) discussed the relation between the gradient of boundary layer entropy and the strengths of the monsoon circulation. In contrast to the ocean, where the boundary layer entropy is primary controlled by the SST, over the continent, surface fluxes are the most important factor, which in turn are strongly affected by radiative forcing. These possible effects emphasize the importance to further investigate this phenomenon and its implications for the WAM circulation and its prediction.

TABLE A1. Verification measures for the final set of experiments of the sensitivity study (see section 3). The table contains one column per variable and six rows per configuration. $SS_{CL}$ is a combination of skill scores for FBIAS, PSS, and COR2; $SS_{conti}$ is a combination of skill scores for BIAS, RMSE, COR1, and COR2; and $SS_{mean}$ is a weighted average of $SS_{CL}$ and all $SS_{conti}$ (see appendix).

| Configuration | | CL (%) | | MSLP (hPa) | $Q_{2m}$ (g kg$^{-1}$) | $T_{2m}$ (°C) | $FF_{10m}$ (m s$^{-1}$) | $FF_{max}$ (m s$^{-1}$) | $LW_{down}$ (W m$^{-2}$) | $SW_{down}$ (W m$^{-2}$) | Mean score |
|---|---|---|---|---|---|---|---|---|---|---|---|
| Observation | $O_{Rate}$ | 58.5 | $O_{Mean}$ | 1013.29 | 17.04 | 25.70 | 2.86 | 6.30 | 415.8 | 178.3 | |
| Noah/Lin | $F_{Rate}$ | 59.3 | $F_{Mean}$ | 1014.14 | 15.51 | 23.80 | 3.85 | 6.81 | 410.5 | 183.5 | |
| | FBIAS | 1.01 | BIAS | 0.84 | −1.53 | −1.89 | 0.98 | 0.51 | −5.3 | 5.2 | |
| | PSS | 0.288 | RMSE | 1.43 | 3.01 | 3.11 | 2.15 | 2.95 | 17.4 | 127.5 | |
| | | | CORR1 | 0.820 | 0.060 | 0.572 | 0.405 | 0.406 | 0.292 | 0.849 | |
| | CORR2 | 0.851 | CORR2 | 0.938 | 0.408 | 0.952 | 0.400 | 0.608 | 0.740 | 0.995 | |
| | Score | 61.07 | Score | −75.60 | −31.99 | −52.24 | −19.76 | −68.49 | 15.90 | −6.82 | 17.50 |
| Noah/MOR2 | $F_{Rate}$ | 59.5 | $F_{Mean}$ | 1014.15 | 15.47 | 23.72 | 3.83 | 6.68 | 410.6 | 173.4 | |
| | FBIAS | 1.02 | BIAS | 0.86 | −1.58 | −1.98 | 0.97 | 0.38 | −5.2 | −4.9 | |
| | PSS | 0.240 | RMSE | 1.44 | 3.03 | 3.14 | 2.16 | 2.79 | 17.4 | 127.0 | |
| | | | CORR1 | 0.818 | 0.057 | 0.570 | 0.398 | 0.461 | 0.299 | 0.845 | |
| | CORR2 | 0.852 | CORR2 | 0.935 | 0.414 | 0.946 | 0.357 | 0.688 | 0.798 | 0.995 | |
| | Score | 59.78 | Score | −75.99 | −31.95 | −54.58 | −21.49 | −55.91 | 22.17 | −13.63 | 18.22 |
| RUC/Lin | $F_{Rate}$ | 67.0 | $F_{Mean}$ | 1014.23 | 16.46 | 23.16 | 3.67 | 6.57 | 412.0 | 167.4 | |
| | FBIAS | 1.15 | BIAS | 0.93 | −0.58 | −2.53 | 0.81 | 0.27 | −3.8 | −10.9 | |
| | PSS | 0.243 | RMSE | 1.50 | 2.90 | 3.47 | 2.02 | 2.73 | 16.8 | 129.3 | |
| | | | CORR1 | 0.813 | 0.046 | 0.500 | 0.412 | 0.448 | 0.241 | 0.834 | |
| | CORR2 | 0.847 | CORR2 | 0.915 | 0.421 | 0.872 | 0.392 | 0.648 | 0.799 | 0.992 | |
| | Score | 48.94 | Score | −77.39 | −30.95 | −83.98 | −18.78 | −46.16 | 26.35 | −39.07 | 10.51 |
| RUC/MOR2 | $F_{Rate}$ | 68.0 | $F_{Mean}$ | 1014.25 | 16.40 | 23.09 | 3.66 | 6.56 | 412.3 | 157.5 | |
| | FBIAS | 1.16 | BIAS | 0.96 | −0.64 | −2.60 | 0.79 | 0.26 | −3.5 | −20.7 | |
| | PSS | 0.239 | RMSE | 1.51 | 2.89 | 3.53 | 2.03 | 2.87 | 16.7 | 132.8 | |
| | | | CORR1 | 0.812 | 0.048 | 0.493 | 0.403 | 0.411 | 0.262 | 0.824 | |
| | CORR2 | 0.832 | CORR2 | 0.909 | 0.423 | 0.848 | 0.344 | 0.638 | 0.819 | 0.991 | |
| | Score | 45.24 | Score | −77.69 | −30.72 | −93.17 | −20.68 | −46.73 | 30.05 | −58.02 | 6.34 |
| PX/Lin | $F_{Rate}$ | 44.4 | $F_{Mean}$ | 1013.60 | 16.58 | 24.74 | 3.42 | 6.18 | 412.7 | 211.3 | |
| | FBIAS | 0.76 | BIAS | 0.30 | −0.47 | −0.96 | 0.56 | −0.11 | −3.1 | 33.0 | |
| | PSS | 0.256 | RMSE | 1.10 | 2.27 | 1.90 | 1.84 | 2.83 | 15.7 | 125.6 | |
| | | | CORR1 | 0.848 | 0.242 | 0.737 | 0.488 | 0.435 | 0.424 | 0.876 | |
| | CORR2 | 0.799 | CORR2 | 0.971 | 0.799 | 0.994 | 0.588 | 0.774 | 0.817 | 0.997 | |
| | Score | 34.76 | Score | −37.80 | −6.41 | −10.30 | −8.90 | −33.44 | 37.25 | −32.05 | 11.87 |

TABLE A1. (*Continued*)

| Configuration | | CL (%) | | MSLP (hPa) | $Q_{2m}$ (g kg$^{-1}$) | $T_{2m}$ (°C) | FF$_{10m}$ (m s$^{-1}$) | FF$_{max}$ (m s$^{-1}$) | LW$_{down}$ (W m$^{-2}$) | SW$_{down}$ (W m$^{-2}$) | Mean score |
|---|---|---|---|---|---|---|---|---|---|---|---|
| PX/MOR2 | $F_{Rate}$ | 45.4 | $F_{Mean}$ | 1013.61 | 16.56 | 24.70 | 3.41 | 6.19 | 413.5 | 195.1 | |
| | FBIAS | 0.78 | BIAS | 0.32 | −0.48 | −1.00 | 0.54 | −0.10 | −2.3 | 16.8 | |
| | PSS | 0.261 | RMSE | 1.09 | 2.27 | 1.91 | 1.85 | 2.72 | 15.2 | 118.6 | |
| | | | CORR1 | 0.848 | 0.248 | 0.739 | 0.483 | 0.490 | 0.447 | 0.872 | |
| | CORR2 | 0.821 | CORR2 | 0.974 | 0.798 | 0.994 | 0.565 | 0.809 | 0.810 | 0.995 | |
| | Score | 39.37 | Score | −33.82 | −6.32 | −10.05 | −9.82 | −31.57 | 40.93 | −25.13 | 15.84 |

*Acknowledgments.* RS acknowledges financial support through the MIKLIP VESPA project (BMBF Grant 01LP1110B). The model simulations were made possible through the Cologne High Efficiency Operating Platform for Sciences (CHEOPS, HPC cluster at the RRZK, University of Cologne, Cologne, Germany; http://rrzk.uni-koeln.de/cheops.html). Surface radiation measurements were made possible under the IMPETUS project (BMBF Grant 01LW06001A, North Rhine-Westphalia Grant 313-21200200). The ceilometers and the UHF profiler data at Djougou were obtained from the AMMA database at http://database.amma-international.org/. We acknowledge the Principal Investigators Bernhard Pospichal and Susanne Crewell, and Bernard Campistron, respectively. The AMMA Radiosonde campaign was funded by the EU FP6 AMMA project (Grant 004089) and radiosonde data were taken from the AMMA Radiosonde archive in Cologne. We are grateful to Charles Yorke from the Ghana Meteorological Agency and Francis Didé from the Beninese Weather Service for providing missing synoptic data from their respective countries. Finally we thank three anonymous reviewers for their comments that greatly helped to improve earlier versions of this paper.

## APPENDIX

### Scores Used in the Sensitivity Study

A skill score (SS) is used to compare the skill of a forecast to the skill of a reference in this study to the skill of the ECMWF AMMA reanalysis. The calculation of most skill scores is based on Eq. (A1) (e.g., Jolliffe and Stephenson 2003):

$$\mathrm{SS} = \frac{\mathrm{Score} - \mathrm{Score}_{\mathrm{Ref}}}{\mathrm{Score}_{\mathrm{Perf}} - \mathrm{Score}_{\mathrm{Ref}}} \times 100\% . \qquad \text{(A1)}$$

In Eq. (A1) $\mathrm{Score}_{\mathrm{Ref}}$ is the score of the reference with respect to observations and $\mathrm{Score}_{\mathrm{Perf}}$ is the score of a perfect forecast. Such a SS was calculated for all measures used in this study: FBIAS, systematical error (BIAS), PSS, root-mean-square error (RMSE), correlation between all value pairs (COR1), and correlation between the observed and forecast diurnal cycle (COR2). In addition, the correlation between the diurnal cycle of the observed and forecasted frequency of the event were calculated ($O_{\mathrm{Rate}}$ and $F_{\mathrm{Rate}}$, respectively). Some of the observations used for the calculation of the scores were also assimilated into the reanalysis; their score is therefore close to perfect for some variables and considerably better than the score of WRF, where no observations were assimilated. SS was therefore limited to $-100\%$ to ensure that single variables are not overweighted in the combined SS, which is defined in Eqs. (A2) and (A3):

$$\mathrm{SS}_{\mathrm{CL}} = \frac{2\mathrm{SS}_{\mathrm{FBIAS}} + \mathrm{SS}_{\mathrm{PSS}} + 2\mathrm{SS}_{\mathrm{COR2}}}{5} \quad \text{and} \qquad \text{(A2)}$$

$$\mathrm{SS}_{\mathrm{conti}} = \frac{2\mathrm{SS}_{\mathrm{BIAS}} + \mathrm{SS}_{\mathrm{RMSE}} + \mathrm{SS}_{\mathrm{COR1}} + 2\mathrm{SS}_{\mathrm{COR2}}}{6}, \qquad \text{(A3)}$$

where $\mathrm{SS}_{\mathrm{CL}}$ is the combined skill score calculated for the binary event "low-cloud fraction > 50%" and $\mathrm{SS}_{\mathrm{conti}}$ is the combined skill score calculated for the continuous variables. The weights of the included SSs are chosen to focus more on the reproduction of the observed climatology than on the day-to-day variability. An example of these scores for one experiment is given in Table A1. Finally, the combined skill scores are averaged to obtain a summary score. The weights of this average are subjectively chosen to focus on the cloud formation: NLLJ wind speed, LW and SW radiation are double weighted; MSLP, $Q_{2\mathrm{m}}$, $T_{2\mathrm{m}}$, and $\mathrm{FF}_{10\mathrm{m}}$ are half weighted; CL is weighted with the factor of 8, which is the same as the other variables combined. This mean score is given in the last column of Table A1; it was used to choose the best-performing model configuration in section 3.

## REFERENCES

Abdou, K., D. J. Parker, B. Brooks, N. Kalthoff, and T. Lebel, 2010: The diurnal cycle of lower boundary-layer wind in the West African monsoon. *Quart. J. Roy. Meteor. Soc.,* **136,** 66–76, doi:10.1002/qj.536.

Agustí-Panareda, A., and Coauthors, 2010: The ECMWF re-analysis for the AMMA observational campaign. *Quart. J. Roy. Meteor. Soc.,* **136,** 1457–1472, doi:10.1002/qj.662.

Bain, C. L., D. J. Parker, C. M. Taylor, L. Kergoat, and F. Guichard, 2010: Observations of the nocturnal boundary layer associated with the West African monsoon. *Mon. Wea. Rev.,* **138,** 3142–3156.

Baldi, M., G. A. Dalu, and R. A. Pielke, 2008: Vertical velocities and available potential energy generated by landscape variability—Theory. *J. Appl. Meteor. Climatol.,* **47,** 397–410.

Blackadar, A. K., 1957: Boundary layer wind maxima and their significance for the growth of nocturnal inversions. *Bull. Amer. Meteor. Soc.,* **38,** 283–290.

Boko, M., and Coauthors, 2007: Africa. *Climate Change 2007: Impacts, Adaptation and Vulnerability,* M. L. Parry et al., Eds., Cambridge University Press, 433–467.

Bonner, W. D., and F. Winninghoff, 1969: Satellite studies of clouds and cloud bands near the low-level jet. *Mon. Wea. Rev.,* **97,** 490–500.

Brandt, P., and Coauthors, 2011: Equatorial upper-ocean dynamics and their interaction with the West African monsoon. *Atmos. Sci. Lett.,* **12,** 24–30, doi:10.1002/asl.287.

Christensen, J. H., and Coauthors, 2007: Regional climate projections. *Climate Change 2007: The Physical Science Basis,* S. Solomon et al., Eds., Cambridge University Press, 848–940.

Druyan, L. M., 2011: Studies of 21st-century precipitation trends over West Africa. *Int. J. Climatol.,* **31,** 1415–1424, doi:10.1002/joc.2180.

Eltahir, E. A. B., and C. Gong, 1996: Dynamics of wet and dry years in West Africa. *J. Climate,* **9,** 1030–1042.

Fink, A. H., and Coauthors, 2011: Operational meteorology in West Africa: Observational networks, weather analysis and forecasting. *Atmos. Sci. Lett.,* **12,** 135–141, doi:10.1002/asl.324.

Garcia-Carreras, L., D. J. Parker, and J. H. Marsham, 2011: What is the mechanism for the modification of convective cloud distributions by land surface–induced flows? *J. Atmos. Sci.,* **68,** 619–634.

Grabowski, W. W., and Coauthors, 2006: Daytime convective development over land: A model intercomparison based on LBA observations. *Quart. J. Roy. Meteor. Soc.,* **132,** 317–344, doi:10.1256/qj.04.147.

Grell, G. A., and D. Dévényi, 2002: A generalized approach to parameterizing convection combining ensemble and data assimilation techniques. *Geophys. Res. Lett.,* **29,** doi:10.1029/2002GL015311.

Gultepe, I., M. D. Müller, and Z. Boybeyi, 2006: A new visibility parameterization for warm-fog applications in numerical weather prediction models. *J. Appl. Meteor. Climatol.,* **45,** 1469–1480.

Haywood, J. M., 2005: Can desert dust explain the outgoing longwave radiation anomaly over the Sahara during July 2003? *J. Geophys. Res.,* **110,** D05105, doi:10.1029/2004JD005232.

Hong, S.-Y., H.-M. H. Juang, and Q. Zhao, 1998: Implementation of prognostic cloud scheme for a regional spectral model. *Mon. Wea. Rev.,* **126,** 2621–2639.

Jacoby-Koaly, S., B. Campistron, S. Bernard, B. Bénech, F. Ardhuin-Girard, J. Dessens, E. Dupont, and B. Carissimo, 2002: Turbulent dissipation rate in the boundary layer via UHF wind profiler doppler spectral width measurements. *Bound.-Layer Meteor.,* **103,** 361–389, doi:10.1023/A:1014985111855.

Jolliffe, I. T., and D. B. Stephenson, 2003: *Forecast Verification: A Practitioner's Guide in Atmospheric Science*. Wiley, 240 pp.

Knippertz, P., A. H. Fink, R. Schuster, J. Trentmann, J. M. Schrage, and C. Yorke, 2011: Ultra-low clouds over the southern West African monsoon region. *Geophys. Res. Lett.,* **38,** L21808, doi:10.1029/2011GL049278.

Kothe, S., and B. Ahrens, 2010: On the radiation budget in regional climate simulations for West Africa. *J. Geophys. Res.,* **115,** D23120, doi:10.1029/2010JD014331.

Lafore, J.-P., and Coauthors, 2011: Progress in understanding of weather systems in West Africa. *Atmos. Sci. Lett.,* **12,** 7–12, doi:10.1002/asl.335.

Lebel, T., and Coauthors, 2010: The AMMA field campaigns: Multiscale and multidisciplinary observations in the West African region. *Quart. J. Roy. Meteor. Soc.,* **136,** 8–33, doi:10.1002/qj.486.

Lensky, I. M., and D. Rosenfeld, 2008: Clouds-Aerosols-Precipitation Satellite Analysis Tool (CAPSAT). *Atmos. Chem. Phys.,* **8,** 6739–6753, doi:10.5194/acp-8-6739-2008.

Lim, K.-S. S., and S.-Y. Hong, 2010: Development of an effective double-moment cloud microphysics scheme with prognostic cloud condensation nuclei (CCN) for weather and climate models. *Mon. Wea. Rev.,* **138,** 1587–1612.

Lothon, M., F. Saïd, F. Lohou, and B. Campistron, 2008: Observation of the diurnal cycle in the low troposphere of West Africa. *Mon. Wea. Rev.,* **136,** 3477–3500.

Milton, S. F., G. Greed, M. E. Brooks, J. Haywood, B. Johnson, R. P. Allan, A. Slingo, and W. M. F. Grey, 2008: Modeled and observed atmospheric radiation balance during the West African dry season: Role of mineral dust, biomass burning aerosol, and surface albedo. *J. Geophys. Res.,* **113,** D00C02, doi:10.1029/2007JD009741.

Morcrette, J.-J., and Y. Fouquart, 1986: The overlapping of cloud layers in shortwave radiation parameterizations. *J. Atmos. Sci.,* **43,** 321–328.

Nicholson, S. E., 2009: A revised picture of the structure of the ''monsoon'' and land ITCZ over West Africa. *Climate Dyn.,* **32,** 1155–1171, doi:10.1007/s00382-008-0514-3.

Otkin, J. A., and T. J. Greenwald, 2008: Comparison of WRF model-simulated and MODIS-derived cloud data. *Mon. Wea. Rev.,* **136,** 1957–1970.

Paeth, H., and Coauthors, 2011: Progress in regional downscaling of West African precipitation. *Atmos. Sci. Lett.,* **12,** 75–82, doi:10.1002/asl.306.

Parker, D. J., and Coauthors, 2005: The diurnal cycle of the West African monsoon circulation. *Quart. J. Roy. Meteor. Soc.,* **131,** 2839–2860, doi:10.1256/qj.04.52.

——, and Coauthors, 2008: The AMMA radiosonde program and its implications for the future of atmospheric monitoring over Africa. *Bull. Amer. Meteor. Soc.,* **89,** 1015–1027.

Pohle, S., A. H. Fink, S. Giertz, and B. Diekkrüger, 2010: Hydrometeorological measurements in Benin. *Impacts of Global Change on the Hydrological Cycle in West and Northwest Africa,* P. Speth, M. Christoph, and B. Diekkrüger, Eds., Springer Berlin Heidelberg, 108–113.

Pospichal, B., and S. Crewell, 2007: Boundary layer observations in West Africa using a novel microwave radiometer. *Meteor. Z.,* **16,** 513–523, doi:10.1127/0941-2948/2007/0228.

Redelsperger, J.-L., C. D. Thorncroft, A. Diedhiou, T. Lebel, D. J. Parker, and J. Polcher, 2006: African Monsoon Multidisciplinary Analysis: An international research project and field campaign. *Bull. Amer. Meteor. Soc.,* **87,** 1739–1746.

Roudier, P., B. Sultan, P. Quirion, and A. Berg, 2011: The impact of future climate change on West African crop yields: What does the recent literature say? *Global Environ. Change,* **21,** 1073–1083, doi:10.1016/j.gloenvcha.2011.04.007.

Ruti, P. M., and Coauthors, 2011: The West African climate system: A review of the AMMA model inter-comparison initiatives. *Atmos. Sci. Lett.,* **12,** 116–122, doi:10.1002/asl.305.

Schrage, J. M., and A. H. Fink, 2012: Nocturnal continental low-level stratus over tropical West Africa: Observations and possible mechanisms controlling its onset. *Mon. Wea. Rev.,* **140,** 1794–1809.

——, S. Augustyn, and A. H. Fink, 2007: Nocturnal stratiform cloudiness during the West African monsoon. *Meteor. Atmos. Phys.,* **95,** 73–86, doi:10.1007/s00703-006-0194-7.

Skamarock, W. C., and Coauthors, 2008: A description of the Advanced Research WRF version 3. NCAR Tech. Note NCAR/TN-475+STR, 113 pp. [Available online at http://www.mmm.ucar.edu/wrf/users/docs/arw_v3_bw.pdf.]

Stein, T. H. M., D. J. Parker, J. Delanoë, N. S. Dixon, R. J. Hogan, P. Knippertz, R. I. Maidment, and J. H. Marsham, 2011: The vertical cloud structure of the West African monsoon: A 4 year climatology using CloudSat and CALIPSO. *J. Geophys. Res.,* **116,** D22205, doi:10.1029/2011JD016029.

Turner, D. D., and Coauthors, 2007: Thin liquid water clouds: Their importance and our challenge. *Bull. Amer. Meteor. Soc.,* **88,** 177–190.

U.S. National Weather Service, 2010: Rawinsonde observations. National Weather Service Manual 10-1401, 208 pp. [Available online at http://www.nws.noaa.gov/directives/sym/pd01014001curr.pdf.]

van de Wiel, B. J. H., A. F. Moene, G. J. Steeneveld, P. Baas, F. C. Bosveld, and A. A. M. Holtslag, 2010: A conceptual view on inertial oscillations and nocturnal low-level jets. *J. Atmos. Sci.,* **67,** 2679–2689.

Wang, W., and Coauthors, 2011: ARW version 3 modeling system user's guide. NCAR Tech. Note, 362 pp.

WMO, 2010: Manual on codes, international codes, vol. I.1, part A—Alphanumeric codes, World Meteorological Organization Publ. 306, 506 pp.

Xue, Y., and Coauthors, 2010: Intercomparison and analyses of the climatology of the West African Monsoon in the West African Monsoon Modeling and Evaluation project (WAMME) first model intercomparison experiment. *Climate Dyn.,* **35,** 3–27, doi:10.1007/s00382-010-0778-2.

Yamaguchi, T., and D. A. Randall, 2008: Large-eddy simulation of evaporatively driven entrainment in cloud-topped mixed layers. *J. Atmos. Sci.,* **65,** 1481–1504.

Yum, S. S., and J. G. Hudson, 2002: Maritime/continental microphysical contrasts in stratus. *Tellus,* **54B,** 61–73, doi:10.1034/j.1600-0889.2002.00268.x.

Zhu, P., B. Albrecht, and J. Gottschalck, 2001: Formation and development of nocturnal boundary layer clouds over the Southern Great Plains. *J. Atmos. Sci.,* **58,** 1409–1426.